NANO LETTERS

Letter

pubs.acs.org/NanoLett

Ultracompact Silicon-Conductive Oxide Nanocavity Modulator with 0.02 Lambda-Cubic Active Volume

Erwen Li,[†] Qian Gao,[†] Ray T. Chen,[‡] and Alan X. Wang*,[†]

[†]School of Electrical Engineering and Computer Science, Oregon State University, Corvallis, Oregon 97331, United States

[‡]Department of Electrical and Computer Engineering, The University of Texas at Austin, Austin, Texas 78758, United States

S *Supporting Information*

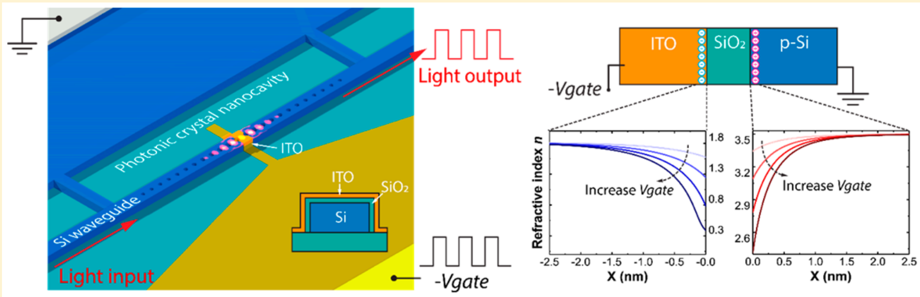

ABSTRACT: Silicon photonic modulators rely on the plasma dispersion effect by free-carrier injection or depletion, which can only induce moderate refractive index perturbation. Therefore, the size and energy efficiency of silicon photonic modulators are ultimately limited as they are also subject to the diffraction limit. Here we report an ultracompact electro-optic modulator with total device footprint of $0.6 \times 8\ \mu m^2$ by integrating voltage-switched transparent conductive oxide with one-dimensional silicon photonic crystal nanocavity. The active modulation volume is only 0.06 um^3, which is less than 2% of the lambda-cubic volume. The device operates in the dual mode of cavity resonance and optical absorption by exploiting the refractive index modulation from both the conductive oxide and the silicon waveguide induced by the applied gate voltage. Such a metal-free, hybrid silicon-conductive oxide nanocavity modulator also demonstrates only 0.5 dB extra optical loss, moderate Q-factor above 1000, and high energy efficiency of 46 fJ/bit. The combined results achieved through the holistic design opened a new route for the development of next generation electro-optic modulators that can be used for future on-chip optical interconnects.

KEYWORDS: *Silicon photonics, transparent conductive oxides, optical modulator, photonic crystal cavity, plasmonics*

The ever-increasing demand to process, store, and exchange information creates an unceasing driving force for high-bandwidth, energy-efficient photonic technologies. In recent years, the vision to develop photonic devices with extremely high energy efficiency to attojoule/bit has been outlined.[1,2] Silicon photonics has the potential to transform future optical interconnect systems by reducing the energy consumption and enhancing the bandwidth of existing electronic systems by orders of magnitude using complementary metal-oxide-semiconductor (CMOS) compatible fabrication processes.[3−5] For example, silicon electro-optic (E-O) modulators have been reported with femtojoule/bit energy efficiency.[6,7] In addition to the application in optical interconnects, silicon photonic devices can also operate the logic gates to conduct certain types of optical computation.[8−10] However, the performance of silicon photonic devices is still limited by the diffraction limit and the relatively weak plasma dispersion effect. Although silicon has a relatively high refractive index, it can only shrink the wavelength inside the silicon waveguide proportionally to the scale of λ/n, roughly to 400−600 nm. Further reduction of the device footprint requires exploiting surface plasmon polaritons (SPPs), which are bound waves at the interface between a metal and a dielectric.[11] The extremely strong light confinement of metal−insulator−metal (MIM) waveguide has led to the demonstration of ultracompact and high-bandwidth plasmonic E-O modulators.[12,13] However, plasmonic structures and devices are very lossy and can only carry information over a very short distance. Therefore, hybrid plasmonic-dielectric waveguide integration must be used for real optical interconnects,[12] which increases the complexity of design and fabrication.

The second constraint of silicon photonic devices is the plasma dispersion effect induced by free-carrier injection or depletion,[12] which can only induce moderate refractive index perturbation. For example, for a typical depletion-based silicon photonic modulator with a moderate doping level of 2.5×10^{18} cm^{-3} in its active region,[6] when it is completely depleted, the refractive index only changes by 0.06%. As a result, current Mach−Zehnder interferometer (MZI) silicon modulators require a long device length up to hundreds of micrometers

Received: October 27, 2017
Revised: January 3, 2018
Published: January 8, 2018

DOI: 10.1021/acs.nanolett.7b04588
Nano Lett. XXXX, XXX, XXX−XXX

to several millimeters to accumulate sufficient phase modulation.[14] The large device footprint also leads to a large energy consumption of picojoule/bit, which cannot meet the requirement of future photonic interconnects application. Compared with MZI modulators, resonator-based E-O modulators occupy a much smaller footprint and achieve significantly higher energy efficiency. To date, various ultracompact silicon microring resonators,[15−17] microdisks resonators,[6,18] and photonic crystal nanocavity[19] have been demonstrated and used in optical interconnect systems, achieving high performance in modulation speed, compactness, and energy efficiency. However, resonator-based modulators have an intrinsic trade-off between energy efficiency and optical bandwidth. For practical devices, thermal control with integrated heater and temperature sensors are often used to obtain stable performance,[20,21] but with the sacrifice of additional energy consumption and footprint.

To overcome the intrinsic drawback of the plasma dispersion effect of silicon, various functional materials, such as graphene,[22,23] vanadium oxide,[24] and ferroelectric materials[25] have been integrated with silicon photonics to build next generation E-O modulators. Among all these emerging materials, transparent conductive oxides (TCOs) have attracted escalating interests as a new type of plasmonic material[26,27] and as active materials for E-O modulators[28−31] in recent years due to the large tunability of their refractive indices. TCOs, such as indium−tin oxide (ITO) and aluminum−zinc oxide (AZO), are a family of wide-bandgap semiconductor oxide materials that can be degenerately doped to a high level, which is widely used in the display industry.[32] With free-carrier concentrations ranging from 1×10^{19} to 1×10^{21} cm^{-3}, the real part n of the refractive index could experience more than 1 refractive index unit (RIU) change,[33] as shown in Figure 1a. Meanwhile, the imaginary part κ increases to the same order of magnitude as the real part, which causes dramatic increase of the absorption 30−140× larger than that of silicon, as shown in Figure 1b. In recent years, a unique property called epsilon-near-zero (ENZ) is verified with TCO materials.[34,35] At very high free-carrier concentration, the real permittivity of TCOs reaches zero while the absolute permittivity is a minimum value due to the small value of the imaginary part as indicated by the vertical dotted lines in Figure 1c,d. In this case, the electric field will be strongly confined in TCOs due to the continuity of electric field displacement at the material interface. ENZ will further enhance the light−matter interaction as discussed in ref 36. For silicon, however, it is still far from ENZ even at 10^{21} cm^{-3} free-carrier concentration due to the large value of its high frequency permittivity.

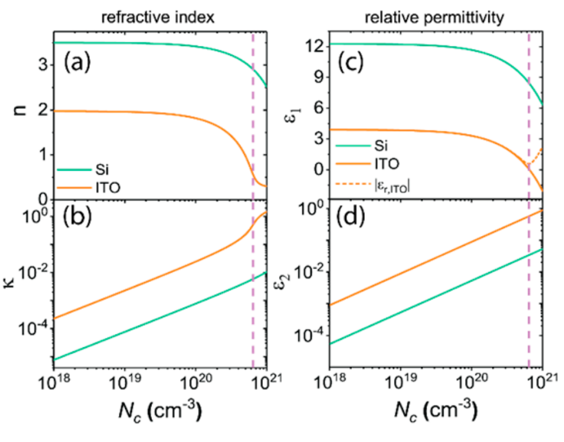

Figure 1. (a) Real part (n) and (b) imaginary part (κ) of the refractive indices of p-type Si (green solid) and ITO (orange solid) as a function of free-carrier concentration N_c (hole in Si, $N_{h,Si}$; and electron in ITO, $N_{e,ITO}$) at wavelength $\lambda = 1.55$ μm. (See the Supporting Information for calculation details.) (c) Real part (ε_1) and (d) imaginary part (ε_2) of the relative permittivity of p-type Si (green solid line) and ITO (orange solid line) as a function of N_c at wavelength $\lambda = 1.55$ μm. The orange dashed line in part c shows the absolute permittivity of ITO ($|\varepsilon_{r,ITO}|$), and the pink dashed line indicates the N_c where the ITO reaches ENZ.

Existing TCO-based E-O modulators are exclusively based on straight silicon waveguide[28−30] or plasmonic slot waveguide[31] using electrically induced optical absorption from the integrated MOS capacitor. The phase change induced by the real part of the permittivity of the TCO materials, although automatically accompanying the imaginary part of the index change, does not contribution to any E-O modulation. Therefore, a relatively long modulation length (a few microns) is required to induce sufficient optical absorption. Moreover, these TCO modulators require the presence of metal gates for strong plasmonic light confinement and electronic signal conductance, which introduce relatively high optical loss even at the transparent state. In this manuscript, we present an ultracompact hybrid silicon-TCO nanocavity modulator to overcome the intrinsic drawbacks of those straight waveguide modulators. There are two exclusive advantages compared with existing TCO-based modulators. First, the active region of our plasmonic E-O modulator is free of metal. The metal gate of the MOS capacitor is replaced by an ITO gate, which induces much smaller optical absorption compared with other metal-gated modulators. This ITO−oxide−Si capacitor offers the possibility to build a relatively high Q-factor resonator while traditional metal−oxide−ITO cannot. Second, in our nanocavity E-O modulator, both the phase change and the absorption, from both the Si and ITO materials, will contribute coherently to E-O modulation. The total device footprint of our TCO modulator is only 0.6×8 μm^2 using one-dimensional (1D) photonic crystal (PC) nanocavity with 20 nm SiO_2 as the insulator and 20 nm ITO as the gate. The E-O modulation volume is less than 0.06 μm^3 (width × height × length = 0.56 μm × 0.28 μm × 0.375 μm), namely, only 2% of lambda-cubic ($0.02\lambda^3$) volume, which is the smallest active modulation region that has ever been reported to the best of our knowledge. The E-O modulation volume is the most critical device metric that affects the energy efficiency of an E-O modulator,[1] which is usually achieved by compact resonant cavities or plasmonic structures. A few ultracompact resonator-based E-O modulators have been reported, including microdisk modulators[6,18] using vertical p−n junction with an active volume of 1.6−2.5 μm^3 and p−i−n photonic crystal nanocavity modulator[19] with a modulation volume of 2.2 μm^3. Non-resonator-type TCO plasmonic modulators have typical lengths of 5 μm[30] to 10 μm[31] long, with calculated active modulation volume around 0.6 μm^3. Our device combines the advantages of ultracompact resonators and TCO plasmonics, which further reduces the active E-O modulation volume by 10×.

Briefly, the applied gate voltage induces free electron and hole accumulation ITO and silicon, respectively. The free-carrier-induced variation of the real part of the optical permittivity causes blue-shift of the resonance peak, while the increase of the imaginary part of the optical permittivity induces optical absorption of the resonance mode, which becomes more prominent when ITO is close to ENZ. We experimentally

DOI: 10.1021/acs.nanolett.7b04588
Nano Lett. XXXX, XXX, XXX−XXX

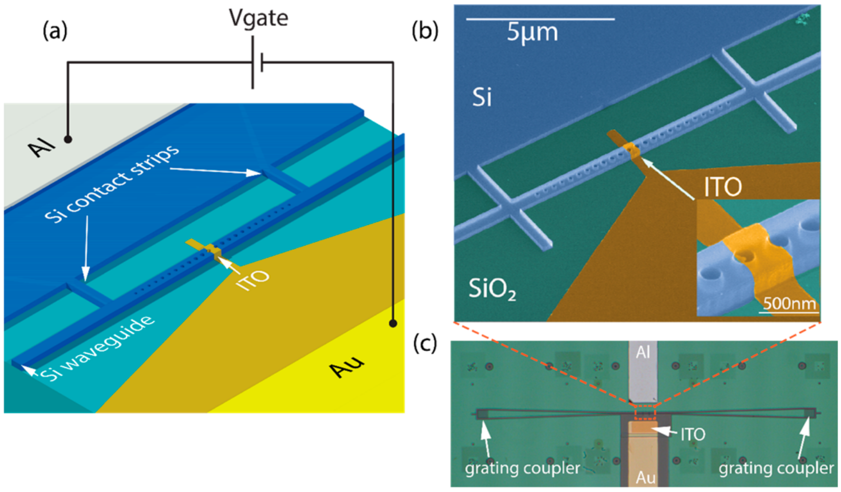

Figure 2. (a) 3D schematic of the Si-ITO modulator. (b) Colored scanning electron micrograph (SEM) of the fabricated Si-ITO modulator. The insertion figure shows the zoomed-in view of the center of the MOS capacitor region. (c) Optical image of the fabricated modulator.

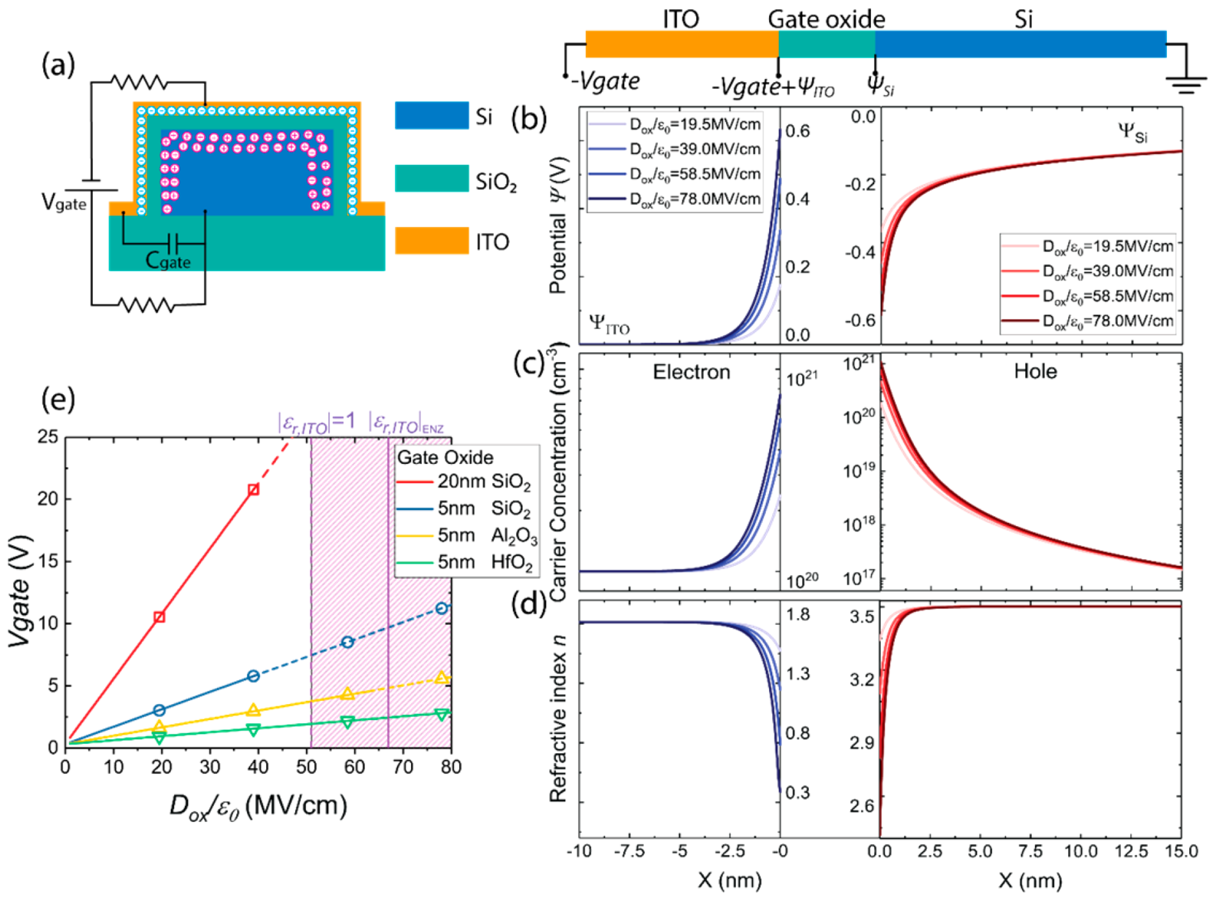

Figure 3. (a) Cross-section of the Si/oxide/ITO MOS capacitor at the center of the hybrid Si-ITO modulator. When a negative bias is applied on the ITO gate, electrons and holes accumulate at the ITO/oxide and Si/oxide interfaces, respectively. (b) Electrical potential distribution in ITO (blue lines) and Si (red lines) as a function of electrical displacement field in the gate oxide layer, D_{ox}. (c) Carrier density distribution in ITO (electron) and Si (hole) as a function of D_{ox} field. (d) The real part refractive index (n) distribution in ITO and Si as a function of D_{ox} field. (e) Gate voltage as a function of the D_{ox} field for different gate oxide layers: 20 nm SiO_2 (red line), 5 nm SiO_2 (blue line), 5 nm Al_2O_3 (yellow line), and 5 nm HfO_2 (green line). The dashed lines show the D_{ox} field range when the gate oxide layer will breakdown. The shaded area enclosed by the purple dashed line shows the D_{ox} field range when the permittivity of ITO accumulation layer, $|\varepsilon_{r,ITO}|$, is smaller than 1, representing the ENZ region; the purple solid line indicates the D_{ox} field when $|\varepsilon_{r,ITO}|$ reaches minimum ENZ value.

achieved a large E-O response of 30 pm/V and high energy efficiency of 46 fJ/bit. Compared with those of reported TCO-based plasmonic modulators, the active region of our device is completely free of metallic materials, which offers a low device loss of only 0.5 dB, moderately high Q-factor of 1000, and better compatibility with CMOS processes. Compared with the

DOI: 10.1021/acs.nanolett.7b04588
Nano Lett. XXXX, XXX, XXX−XXX

conventional silicon ring resonator or microdisk modulator, our device shows exclusive advantages as it provides a larger resonant wavelength tuning and much higher usable optical bandwidth of greater than 1 nm. Through future research by replacing the current SiO_2 gate with high-k materials and improving the Q-factor, we can potentially achieve even higher energy efficiency below 1 fJ/bit.

The schematic of the ITO-gated 1D silicon PC nanocavity is shown in Figure 2a. The device consists of a MOS capacitor built at the center of the nanocavity on a silicon strip waveguide. The strip waveguide is fabricated on a p-type silicon-on-insulator (SOI) substrate with 500 nm in width and 250 nm in height. A pair of grating couplers are integrated to couple light in and out of an optical fiber. The PC cavity is defined through electron beam lithography (EBL) and reactive ion etching (RIE), operating in the TE mode. Two photonic crystal mirror segments are placed back-to-back adjacent to the nanocavity. The air hole size is quadratically tapered down from the center of the cavity region to the edge of the two mirror segments. In our design, each mirror segment has 12 air holes. The filling factor, which is defined as $f = A/pw$, is tapered down from 0.23 in the center to 0.1 at the edge, where A is the air hole area, p is the air hole period, and w is the waveguide width. The period p is chosen to be 340 nm to allow the modulator to operate in the telecommunications wavelength range. In the center of the cavity, an ITO/SiO_2/Si film stack creates a MOS capacitor with cross-sectional view shown in Figure 3a. Here, the silicon waveguide also serves as the bottom electrode despite its relatively high resistivity. Two 400 nm wide silicon strips are used to form the conduction path between the silicon waveguide and the silicon slab with the contact electrodes. Then, a 20 nm thick SiO_2 layer is thermally grown on top of the entire silicon PC nanocavity serving as the gate oxide. Finally, a 20 nm thick ITO layer is sputtered, performing as the metallic gate electrode. We need to emphasize that the center nanocavity length is only 120 nm, which is at least 50× shorter than ring resonators or microdisk resonators. A 375 nm long ITO gate is made to compensate the misalignment of the electron beam lithography (EBL) process as shown by the inset figure of Figure 2b. The SEM and optical images of one fabricated device are depicted in Figure 2b,c (see the Supporting Information for details of fabrication).

The device operates in the accumulation mode of the MOS capacitor with the negative gate bias on the ITO gate. Unlike other reported TCO-MOS E-O modulators which ignore the free-carrier effect in the metal gate, we consider the free-carrier accumulation at both sides of the interfaces, i.e., in the ITO/SiO_2 and Si/SiO_2 interfaces. We perform a numerical simulation systematically to analyze the carrier distribution in the accumulation layers versus the applied gate bias. In our modeling, the carrier density and electric potential in the ITO and Si regions are treated in different ways. The main difference is that the high doping level of ITO results in an initial Fermi level higher than the bottom of the conduction band. Therefore, the electron density and electric potential in ITO behave more like a metal, which can be approximated by the Thomas−Fermi screening model.[37,38] On the other side, Si follows the classic semiconductor theory.[39] However, a large band bending is expected in our device, and a traditional Boltzmann distribution approximation is not accurate. A rigorous analysis using the Fermi−Dirac distribution is used to model the Si side. In order to obtain representative results, we conduct our modeling using the electric displacement field D_{ox} instead of the electric field E. The boundary condition only requires the value of D_{ox} in the gate oxide layer, making the modeling independent of the gate oxide material and thickness. We plot the electric potential and carrier distribution as a function of D_{ox} as shown in Figure 3b,c. We can see that the electron concentration in ITO ($N_{e,ITO}$) accumulates from 1×10^{20} to 7.46×10^{20} cm^3, and the hole concentration in Si ($N_{h,Si}$) accumulates from 1×10^{17} to 1.08×10^{21} cm^3 with a D_{ox}/ε_0 value of 78 MV/cm. Surprisingly, the peak of $N_{h,Si}$ is even higher than that of $N_{e,ITO}$, which is because of the larger effective density of state of Si compared with that of ITO (see the Supporting Information). As a result, $N_{h,Si}$ in Si is more sensitive to electrical potential modulation than $N_{e,ITO}$ in ITO. The ITO reaches the ENZ region when the $N_{e,ITO}$ is 6.4×10^{20} cm^3 with D_{ox}/ε_0 of 67 MV/cm. Figure 3d plots the corresponding distribution of the refractive indices of ITO and Si. Both ITO and Si exhibit dramatic refractive index modulation within a thin layer of ∼1 nm thick close to the interface even at a relatively small D_{ox} field. For the ITO side, the effect of this thin accumulation layer is already well-recognized.[30,37,38] This layer is often treated as an effective accumulation layer, and the thickness can be estimated by the Thomas−Fermi screening length, L_{tf}. On the Si side, this thin accumulation layer could also play a critical role for the E-O modulation but was not utilized by simple straight waveguides in published papers. Detailed analysis will be provided in the following section. Next, knowing the D_{ox} field, we can calculate the gate voltage by $V_{gate} = |\Psi_{ITO}| + \frac{D_{ox} t_{ox}}{\varepsilon_0 \varepsilon_{oxide,st}} + |\Psi_{Si}|$, where Ψ_{ITO} and Ψ_{Si} are the surface potential at the ITO/SiO_2 and the Si/SiO_2 interface, ε_0 is the vacuum permittivity, and $\varepsilon_{oxide,st}$ and t_{ox} are the static relative permittivity and thickness of the gate oxide layer. Figure 3e plots the applied gate voltage as a function of D_{ox} field with different oxide materials and thicknesses. Here the dashed lines indicate a large D_{ox} field exceeding the breakdown of the gate oxide. From this analysis, it is obvious to draw a conclusion that thinner oxide layer thickness and high-k materials will help to reduce the applied bias voltage. Besides, to truly reach the ENZ operation of the ITO layer, a high-k gate material such as HfO_2 is necessary. In our experimental demonstration, we chose SiO_2 as the gate oxide material primarily due to our current fabrication facilities.

The Si-ITO nanocavity modulator operates in the dual mode of cavity resonance and optical absorption. At a relatively small applied bias, the device operates in the "normal mode", when the $N_{e,ITO}$ is not high enough to push ITO into the ENZ confinement. Modulation of the nanocavity resonance dominates, which mainly comes from the real parts of the permittivity change ($\Delta\varepsilon_1$) induced by the plasma dispersion effect of the ITO and Si. Based on the cavity perturbation theory, the resonance shift ($\Delta\omega$) can be expressed as[40]

$$\Delta\omega = \frac{-\frac{\omega}{2}\int \Delta\varepsilon E^* E \, \mathrm{d}v}{\int \varepsilon E^* E \, \mathrm{d}v}$$

where ω is the original resonance frequency, ε and $\Delta\varepsilon$ are the distribution of the original and changed permittivity, and E is the electric field distribution of the cavity mode. We know that the permittivity change caused by the plasma dispersion is proportional to the change of free-carrier concentration, namely, $\Delta\varepsilon \propto \Delta N_c$. This means that the resonance shift induced by a 1 nm thick accumulation layer with a N_c of 1×10^{20} cm^{-3} is equivalent to the shift induced by a 100 nm thick

DOI: 10.1021/acs.nanolett.7b04588
Nano Lett. XXXX, XXX, XXX−XXX

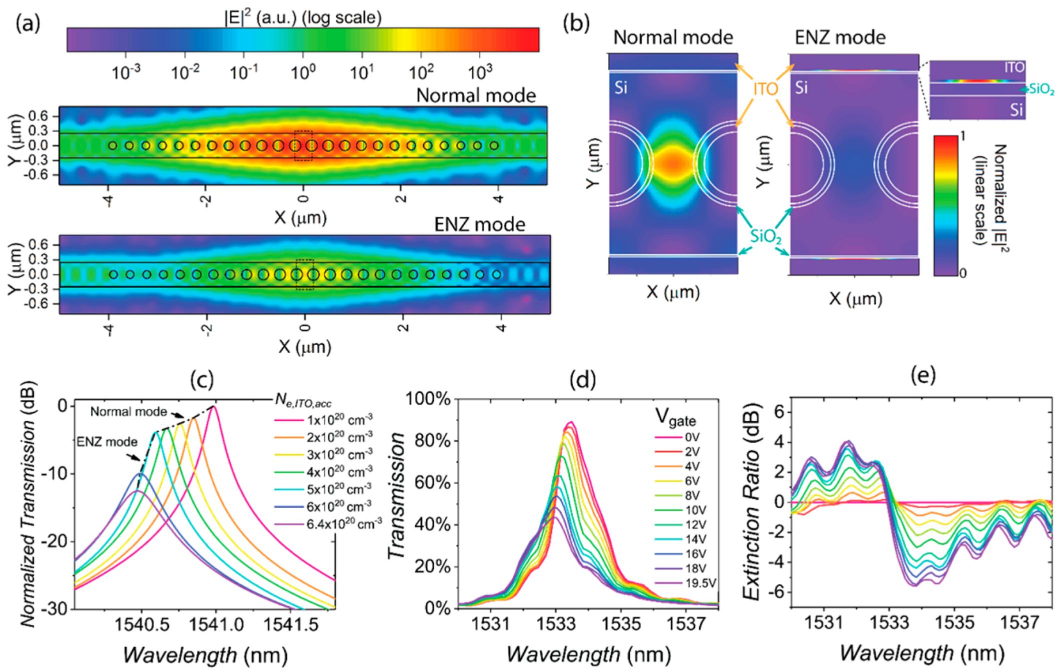

Figure 4. (a) Photonic crystal cavity mode profiles of "normal mode" (accumulation layer $N_{e,ITO}$ = 1 × 10^{20} cm^{-3}) and "ENZ mode" (accumulation layer $N_{e,ITO}$ = 6.4 × 10^{20} cm^{-3}). The optical field intensity is plotted in log scale. Clearly, at "ENZ mode" the transmission drops due to the ITO absorption. (b) Zoomed-in mode profile of "normal mode" and "ENZ mode". The optical intensity is plotted in normalized linear scale. Inset: further zoomed-in mode profile of "ENZ mode" at the ITO/SiO_2 interface. It is clearly shown that in "ENZ mode" the optical field is strongly confined in the accumulation layer at the side wall. (c) Simulated normalized transmission spectrum at different free-carrier concentration $N_{e,ITO,acc}$ in the ITO accumulation region. The black dashed line outlines the change of the transmission peak as $N_{e,ITO}$ increases. (d) Measured static transmission spectrum as a function of the applied bias voltage. The DC applied bias ranges from 0 to 19.5 V. (e) Measured extinction ratio (ER) spectrum as a function of the applied bias voltage.

layer from full depletion to a N_c of 1 × 10^{18} cm^{-3} under the uniform optical field distribution approximation. Figure 4a,b shows the simulated photonic crystal cavity mode profile. The cavity mode has a good overlap with the accumulation layer of the MOS structure near the center air holes and is relatively uniform. Thus, it is reasonable to assume an approximately uniform optical distribution here. The resonance shift has the following relationship:

$$\Delta\omega \propto \frac{\omega \int \Delta N_c \, dv}{\varepsilon_{eff} v_c} = \frac{\omega \Delta Q}{\varepsilon_{eff} v_c} = \frac{\omega CV}{\varepsilon_{eff} v_c} = \frac{\omega CV}{\varepsilon_{eff} \gamma v_a} \propto \frac{C}{v_a}$$

where ε_{eff} and v_c are the effective permittivity and mode volume of the cavity mode, ΔQ is the accumulated free carriers induced by the applied voltage V, C and v_a are the capacitance and volume of the active modulation region of the modulator, respectively, and γ is the coefficient describing the overlapping between v_a and v_c. Additionally, due to the small mode volume of the photonic crystal cavity mode and its large overlap with the active modulation region of the modulator (Figure 4b), we can conclude that the resonance shift is proportional to the capacitance per unit active volume. Large capacitance C and small active volume v_a are preferred for high modulation efficiency. Since we effectively construct a 3D MOS capacitor in the center of the photonic crystal cavity, free carriers accumulate at all three interfaces. As large C/v_a ratio is realized, we can achieve significant resonance modulation within 0.02λ^3 active modulation volume. In spite of the resonance shift induced by the real part permittivity change, the optical absorption from the imaginary part change of the permittivity, which is usually a minor effect in pure silicon modulators, also plays an important role in the Si-ITO hybrid modulator because of the 30−140× larger imaginary part of ITO compared with Si. As a result, larger extinction ratio can be achieved at the same resonance tuning. As the applied bias increases, the accumulation layer of ITO approaches the ENZ region as shown by the shaded area in Figure 3e. Once the modulator reaches the "ENZ mode", the optical mode starts to be confined in the ITO accumulation layer. This ENZ confinement effect is highly polarization sensitive. For our photonic crystal nanocavity design operating in the TE mode, it mainly happens at the sidewall interface as shown in Figure 4b. The ENZ confinement effect will dramatically enhance the absorption which is proportional to $\frac{\varepsilon_{2,ITO}}{2|\varepsilon_{ITO}|^2}$.[41] In this case, the optical absorption mode dominates. Figure 4c plots the simulated transmission spectra of the hybrid Si-ITO modulator at different carrier concentrations in the accumulation region, $N_{e,ITO,acc}$. The black dashed line outlines the evolution of the transmission peak. The trend from the normal resonance modulation to ENZ electroabsorption is clearly shown as $N_{e,ITO}$ increases.

The E-O modulation response of fabricated hybrid Si-ITO modulator was characterized (see the Supporting Information for details of measurement setup). Figure 4d shows the measured transmission spectra as a function of the applied bias. The spectra are normalized to a straight Si waveguide as the reference. The insertion loss (IL) of the PC nanocavity modulator is only 0.5 dB at the peak resonance wavelength. The free-carrier concentration of as-sputtered ITO is 1 × 10^{20} cm^{-3}, which is still a dielectric material at telecommunications wavelengths. The measured Q-factor after ITO deposition is

DOI: 10.1021/acs.nanolett.7b04588
Nano Lett. XXXX, XXX, XXX−XXX

around 1000, which is slightly smaller than the *Q*-factor measured before sputtering the ITO (~1200), proving that the degradation of the *Q*-factor due to the thin ITO layer is minor. The resonance wavelength blue-shifts by 0.57 nm with a change in DC bias from 0 to −19.5 V, indicating a 30 pm/V modulation efficiency. Meanwhile, we observe a significant drop of the peak transmission by 45.34%, which is caused by the resonance shift as well as the optical absorption. The MOS capacitor operation is verified by the low leakage current, which is measured to be less than 100 fA at −20 V. Figure 4e plots the extinction ratio (ER) spectrum as a function of the applied bias. A usable optical bandwidth of greater than 1 nm is observed if we allow 1 dB variation of the ER. The maximum modulation is observed at 1533.78 nm, which introduces an additional loss of 0.75 dB as compared to the peak wavelength. The transmission varies by 5.6 dB with a bias changing from 0 to −19.5 V. The dynamic modulation speed is demonstrated up to 3.2 MHz with an AC voltage swing of 0 to −12 V (as shown in Figure 5), which is limited by our testing instruments.

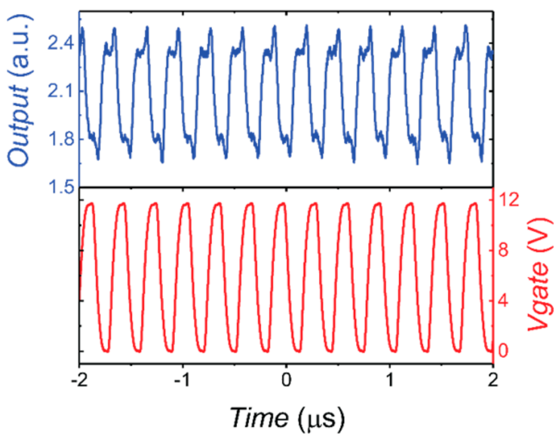

Figure 5. AC optical modulation testing results at 1534.78 nm with 0 to −12 V sweep input bias voltage at 3.2 MHz.

Here we estimated the modulation speed and energy efficiency of the hybrid Si-ITO nanocavity modulator. The speed of the modulator is limited by the RC delay since its operation is based on the fast accumulation mode of a MOS capacitor. The finite element method (FEM) simulation gives the capacitance of the modulator including the whole PC nanocavity and the ITO gate in the active region to be 1.28 fF. The series resistance of our fabricated device is around 4.9 MΩ, which is limited by the lightly doped (1×10^{15} cm^{-3}) SOI slab. Consequently, our current device has a relatively slow RC-limited speed of 160 MHz. However, the series resistance can be reduced to ~9 KΩ by selectively doping the silicon conduction strips and PC waveguide to a high level of 5×10^{18} cm^{-3} while keeping the doping of the center active cavity region at a moderate high level of 1×10^{17} cm^{-3} (see the Supporting Information for details of capacitance and resistance calculation). The optical loss of a passive silicon waveguide with high-level doping is around 0.017 dB/μm according to our optical FEM simulation. A 10 μm long silicon waveguide with high doping level will only introduce an additional loss of 0.17 dB. Besides, the corresponding silicon waveguide loss of moderate high doping level is 3.4×10^{-4} dB/μm. For a cavity with a moderate *Q*-factor of 5000, which corresponds to a photon lifetime of 4.2 ps, the increasing in optical loss is only 0.12 dB. As a result, the RC-limited bandwidth can be improved to 87 GHz. However, the real achievable operation speed will be limited by the electronic circuit or signal generator. The energy efficiency of the modulator is estimated using $E_{\text{per-bit}} = CV^2/4$. Assuming a 12 V voltage swing (3 dB ER at the resonance peak), the energy consumption of the device is only 46 fJ/bit. Since the free-carrier accumulation in the MOS only depends on the *D* field in the gate insulator, the performance of the hybrid silicon-ITO modulator can be further improved with high-*k* materials such as HfO_2. For example, if we replace the 20 nm SiO_2 with 5 nm thick HfO_2, the applied voltage will be reduced to 1 V to achieve the same *D* field using current 12 V bias. In this case, the RC-limited speed will decrease to 40 GHz due to the increased capacitance. However, the resonance tuning efficiency will increase to 360 pm/V, and the energy consumption will drop to 6.2 fJ/bit. In addition, our current hybrid silicon-ITO nanocavity modulator only possesses a moderate *Q*-factor of 1000 due to our fabrication quality such as the surface roughness and the deviation of the air hole diameters. Through advanced designs[42] and optimized fabrication, a PC nanocavity with higher *Q*-factor is achievable. We anticipate that both the ER and the operation voltage will be improved in further development, offering the possibility to achieve hundreds of attojoule/bit energy efficiency in the future. For example, if the *Q*-factor is improved to 5000 (*Q*-factor-limited bandwidth will be 240 GHz), we can further reduce the operational voltage by 5× and improve the energy efficiency by 25× to 250 aJ/bit.

■ ASSOCIATED CONTENT

Supporting Information

The Supporting Information is available free of charge on the ACS Publications website at DOI: 10.1021/acs.nanolett.7b04588.

> Calculation of permittivity and refractive index of ITO and Si, details of electrical modeling of ITO/oxide/Si capacitor, optical simulation, calculation of the capacitance and resistance, experimental details of device fabrication, and measurement setup (PDF)

■ AUTHOR INFORMATION

Corresponding Author

*E-mail: wang@oregonstate.edu.

ORCID

Alan X. Wang: 0000-0002-0553-498X

Author Contributions

A.X.W. and R.T.C. conceived the ideas of the project. E.L. performed the simulations and devised the geometry of the modulators. E.L. and Q.G. fabricated the hybrid Si-ITO modulators. E.L. conducted the optical and electrical characterization of the modulators under the supervision of A.X.W. All authors discussed the results. E.L. and A.X.W. cowrote the paper. R.T.C. and A.X.W. supervised the project.

Notes

The authors declare no competing financial interest.

■ ACKNOWLEDGMENTS

The authors thank Spencer Liverman for his simulation of the device capacitance using FEM and Prof. John F. Wager for the discussion of MOS modeling and the help of ITO sputtering from his group. Simulations have been carried out on the workstations of Prof. Ray T. Chen's group at the University of Texas at Austin. This work is supported by the AFOSR MURI Project FA9550-17-1-0071 under the guidance of Dr. Gernot Pomrenke.

■ REFERENCES

(1) Miller, D. A. *J. Lightwave Technol.* **2017**, *35*, 346−396.

(2) Pan, Z.; Zhang, C.; Subbaraman, H.; Chung, C. J.; Li, Q.; Xu, X.; Zhang, X.; Guo, L. J.; Chen, R. T. In *SPIE OPTO*, February, 2017; International Society for Optics and Photonics.

(3) Soref, R. *IEEE J. Sel. Top. Quantum Electron.* **2006**, *12*, 1678−1687.

(4) Asghari, M.; Krishnamoorthy, A. V. *Nat. Photonics* **2011**, *5*, 268−270.

(5) Rumley, S.; Nikolova, D.; Hendry, R.; Li, Q.; Calhoun, D.; Bergman, K. *J. Lightwave Technol.* **2015**, *33*, 547−562.

(6) Timurdogan, E.; Sorace-Agaskar, C. M.; Sun, J.; Hosseini, E. S.; Biberman, A.; Watts, M. R. *Nat. Commun.* **2014**, *5*, 5008.

(7) Leuthold, J.; Koos, C.; Freude, W. *Nat. Photonics* **2010**, *4*, 535−544.

(8) Tian, Y.; Zhang, L.; Ji, R.; Yang, L.; Zhou, P.; Chen, H.; Ding, J.; Zhu, W.; Lu, Y.; Jia, L.; Fang, Q. *Opt. Lett.* **2011**, *36*, 1650−1652.

(9) Xu, Q.; Soref, R. *Opt. Express* **2011**, *19*, 5244−5259.

(10) Wang, Z.; Ying, Z.; Dhar, S.; Zhao, Z.; Pan, D. Z.; Chen, R. T. In *CLEO: Science and Innovations*, May, 2017; Optical Society of America.

(11) Barnes, W. L.; Dereux, A.; Ebbesen, T. W. *Nature* **2003**, *424*, 824.

(12) Melikyan, A.; Alloatti, L.; Muslija, A.; Hillerkuss, D.; Schindler, P. C.; Li, J.; Palmer, R.; Korn, D.; Muehlbrandt, S.; Van Thourhout, D.; Chen, B. *Nat. Photonics* **2014**, *8*, 229−233.

(13) Haffner, C.; Heni, W.; Fedoryshyn, Y.; Niegemann, J.; Melikyan, A.; Elder, D. L.; Baeuerle, B.; Salamin, Y.; Josten, A.; Koch, U.; Hoessbacher, C. *Nat. Photonics* **2015**, *9*, 525−528.

(14) Watts, M. R.; Zortman, W. A.; Trotter, D. C.; Young, R. W.; Lentine, A. L. *Opt. Express* **2011**, *19*, 21989−22003.

(15) Tanabe, T.; Nishiguchi, K.; Kuramochi, E.; Notomi, M. *Opt. Express* **2009**, *17*, 22505−22513.

(16) Soref, R. A.; Bennett, B. R. *IEEE J. Quantum Electron.* **1987**, *23*, 123−129.

(17) Ding, J.; Chen, H.; Yang, L.; Zhang, L.; Ji, R.; Tian, Y.; Zhu, W.; Lu, Y.; Zhou, P.; Min, R.; Yu, M. *Opt. Express* **2012**, *20*, 7081−7087.

(18) Xu, Q.; Schmidt, B.; Pradhan, S.; Lipson, M. *Nature* **2005**, *435*, 325.

(19) Xiao, X.; Li, X.; Xu, H.; Hu, Y.; Xiong, K.; Li, Z.; Chu, T.; Yu, J.; Yu, Y. *IEEE Photonics Technol. Lett.* **2012**, *24*, 1712−1714.

(20) Reed, G. T.; Mashanovich, G.; Gardes, F. Y.; Thomson, D. J. *Nat. Photonics* **2010**, *4*, 518−526.

(21) DeRose, C. T.; Watts, M. R.; Trotter, D. C.; Luck, D. L.; Nielson, G. N.; Young, R. W. In *Conference on Lasers and Electro-optics*, May, 2010; Optical Society of America.

(22) Liu, M.; Yin, X.; Ulin-Avila, E.; Geng, B.; Zentgraf, T.; Ju, L.; Wang, F.; Zhang, X. *Nature* **2011**, *474*, 64.

(23) Youngblood, N.; Anugrah, Y.; Ma, R.; Koester, S. J.; Li, M. *Nano Lett.* **2014**, *14*, 2741−2746.

(24) Briggs, R. M.; Pryce, I. M.; Atwater, H. A. *Opt. Express* **2010**, *18*, 11192−11201.

(25) Xiong, C.; Pernice, W. H.; Ngai, J. H.; Reiner, J. W.; Kumah, D.; Walker, F. J.; Ahn, C. H.; Tang, H. X. *Nano Lett.* **2014**, *14*, 1419−1425.

(26) Naik, G. V.; Kim, J.; Boltasseva, A. *Opt. Mater. Express* **2011**, *1*, 1090−1099.

(27) Naik, G. V.; Shalaev, V. M.; Boltasseva, A. *Adv. Mater.* **2013**, *25*, 3264−3294.

(28) Ma, Z.; Li, Z.; Liu, K.; Ye, C.; Sorger, V. J. *Nanophotonics* **2015**, *4*, 198−213.

(29) Keeler, G. A.; Geib, K. M.; Serkland, D. K.; Parameswaran, S.; Luk, T. S.; Griñe, A. J.; Ihlefeld, J.; Campione, S.; Wendt, J. R. In *Optical Fiber Communication Conference*, March, 2017; Optical Society of America.

(30) Sorger, V. J.; Lanzillotti-Kimura, N. D.; Ma, R. M.; Zhang, X. *Nanophotonics* **2012**, *1*, 17−22.

(31) Lee, H. W.; Papadakis, G.; Burgos, S. P.; Chander, K.; Kriesch, A.; Pala, R. A.; Peschel, U.; Atwater, H. A. *Nano Lett.* **2014**, *14*, 6463−6468.

(32) Chiang, H. Q.; Wager, J. F.; Hoffman, R. L.; Jeong, J.; Keszler, D. A. *Appl. Phys. Lett.* **2005**, *86*, 013503.

(33) Feigenbaum, E.; Diest, K.; Atwater, H. A. *Nano Lett.* **2010**, *10*, 2111−2116.

(34) Vasudev, A. P.; Kang, J. H.; Park, J.; Liu, X.; Brongersma, M. L. *Opt. Express* **2013**, *21*, 26387−26397.

(35) Park, J.; Kang, J. H.; Liu, X.; Brongersma, M. L. *Sci. Rep.* **2015**, *5*, 15754.

(36) Liberal, I.; Engheta, N. *Nat. Photonics* **2017**, *11*, 149−158.

(37) Melikyan, A.; Lindenmann, N.; Walheim, S.; Leufke, P. M.; Ulrich, S.; Ye, J.; Vincze, P.; Hahn, H.; Schimmel, T.; Koos, C.; Freude, W. *Opt. Express* **2011**, *19*, 8855−8869.

(38) Krasavin, A. V.; Zayats, A. V. *Phys. Rev. Lett.* **2012**, *109*, 053901.

(39) Colinge, J. P.; Colinge, C. A. *Physics of semiconductor devices*; Springer Science & Business Media, 2005.

(40) Meng, B.; Booske, J.; Cooper, R. *IEEE Trans. Microwave Theory Tech.* **1995**, *43*, 2633−2636.

(41) Shi, K.; Lu, Z. *Opt. Commun.* **2016**, *370*, 22−28.

(42) Md Zain, A. R.; Johnson, N. P.; Sorel, M.; Richard, M. *Opt. Express* **2008**, *16*, 12084−12089.

DOI: 10.1021/acs.nanolett.7b04588
Nano Lett. XXXX, XXX, XXX−XXX